Volume 9 | Number 26 | 14 July 2018 | Pages 5691–5862

Chemical Science

rsc.li/chemical-science

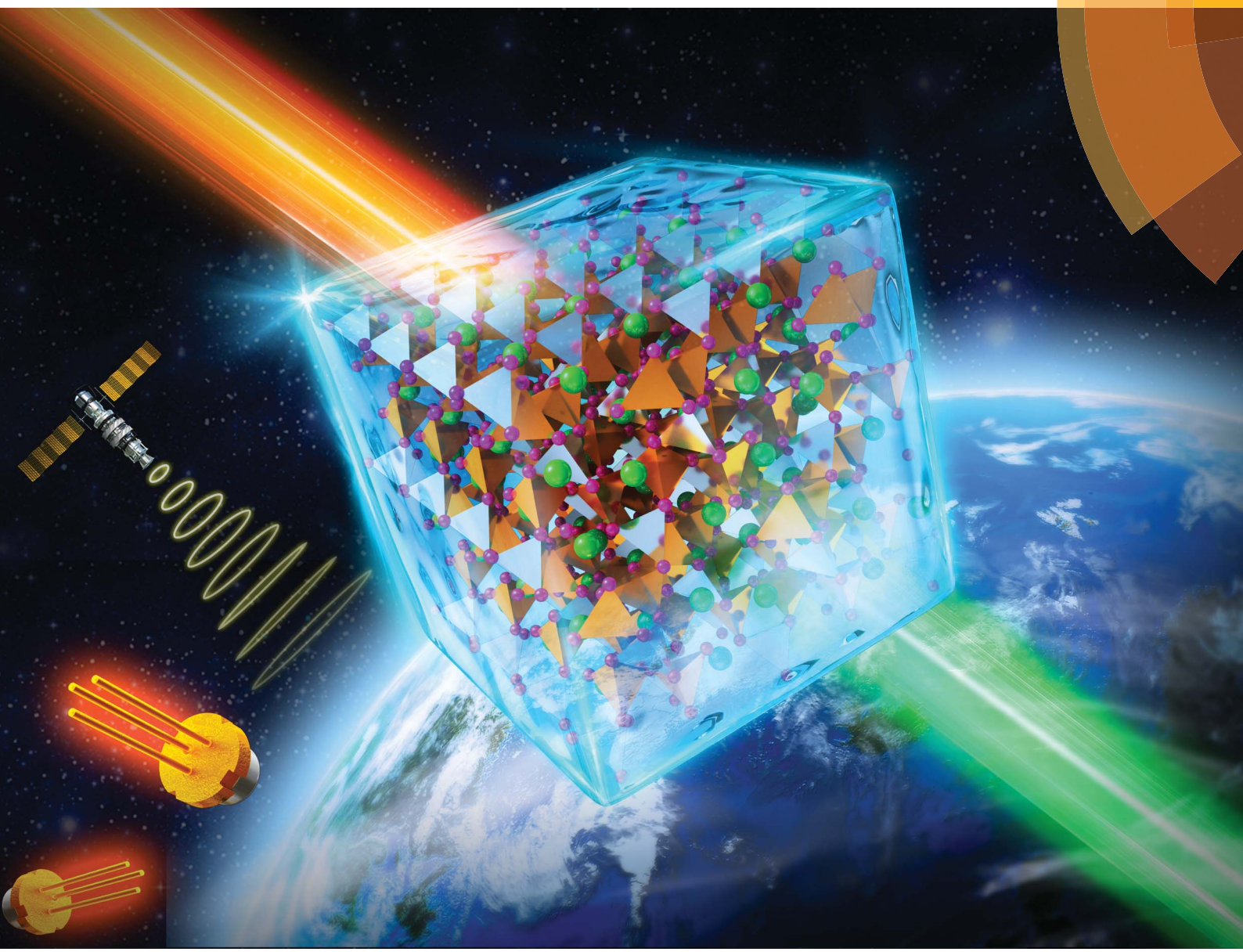

ISSN 2041-6539

ROYAL SOCIETY OF CHEMISTRY

EDGE ARTICLE

Xiao-Ming Jiang, Guo-Cong Guo *et al.*

New strategy for designing promising mid-infrared nonlinear optical materials: narrowing the band gap for large nonlinear optical efficiencies and reducing the thermal effect for a high laser-induced damage threshold

Chemical Science

EDGE ARTICLE

View Article Online
View Journal | View Issue

Cite this: *Chem. Sci.*, 2018, **9**, 5700

New strategy for designing promising mid-infrared nonlinear optical materials: narrowing the band gap for large nonlinear optical efficiencies and reducing the thermal effect for a high laser-induced damage threshold†

Shu-Fang Li,[a] Xiao-Ming Jiang,*[a] Yu-Hang Fan,[b] Bin-Wen Liu,[a] Hui-Yi Zeng[a] and Guo-Cong Guo *[a]

Received 14th March 2018
Accepted 9th May 2018

DOI: 10.1039/c8sc01210e

rsc.li/chemical-science

To circumvent the incompatibility between large nonlinear optical (NLO) efficiencies and high laser-induced damage thresholds (LIDTs) in mid-infrared NLO materials, a new strategy for designing materials with both excellent properties is proposed. This strategy involves narrowing the band gap for large NLO efficiencies and reducing the thermal effect for a high LIDT. To support these proposals, a series of isostructural chalcogenides with various tetrahedral center cations, $Na_2Ga_2MQ_6$ (M = Ge, Sn; Q = S, Se), were synthesized and studied in detail. Compared with the benchmark AGS, these chalcogenides exhibit significantly narrower band gaps (1.56–1.73 eV, AGS: 2.62 eV) and high NLO efficiencies (1.6–3.9 times that of AGS at 1910 nm), and also outstanding LIDTs of 8.5–13.3 × those of AGS for potential high-power applications, which are contrary to the conventional band gap view but can be attributed to their small thermal expansion anisotropy, surmounting the NLO–LIDT incompatibility. These results shed light on the search for practical IR NLO materials with excellent performance not restricted by NLO–LIDT incompatibility.

Introduction

Nonlinear optical (NLO) materials are at the front-line of research in laser science and technology because of their ability to produce coherent and tunable light from solid-state lasers in the medical, military and communication network fields.[1–4] For decades, various NLO materials such as β-BaB_2O_4 (BBO),[5] LiB_3O_5 (LBO),[6] KH_2PO_4 (KDP),[7] $KBe_2B_2O_6F_2$ (KBBF),[8] and $KTiOPO_4$ (KTP)[9] have been discovered and used commercially. Although these materials are applicable to generating coherent light in the ultraviolet region to the near-infrared (IR) region, direct generation of mid-IR (2–20 μm) coherent light by second harmonic generation (SHG) remains particularly challenging, but is crucial to various communication and optoelectronic devices.[10] For decades, numerous mid-IR NLO materials with obvious SHG responses, mainly including pnictides, chalcogenides, and halogenides, have been reported.[11,12] However, only a few of them, namely, $AgGaS_2$ (AGS),[13,14] $AgGaSe_2$ (AGSe),[15,16] and $ZnGeP_2$ (ZGP),[17] can be used. Unfortunately, these materials suffer from drawbacks such as low laser-induced damage thresholds (LIDTs) that hinder their high-power applications.[11] Therefore, developing new mid-IR NLO materials with excellent comprehensive performance (large NLO efficiencies, high LIDT, a wide transparency window, and sufficient birefringence to achieve phase matchability)[18] is technologically and scientifically important.

Among all the requirements for high-power applications, large NLO efficiencies and high LIDTs are the most challenging to achieve concurrently. Previous theoretical and experimental studies on IR NLO materials show that a wider band gap is beneficial for a high LIDT,[1,19,20] while also resulting in a small NLO efficiency, which implies an incompatibility between large NLO efficiencies and high LIDTs. Two main methods have been adopted to balance this conflict. One is increasing the band gap by replacing Ag^+ in the classical IA–IIIA–VIA_2 type of IR NLO material with a strongly electropositive alkali or alkaline-earth metal. Thus, the $LiBQ_2$ (B = Ga, In; Q = S, Se, Te) family and $BaGa_4S_7$ were discovered,[21–25] with their band gaps of up to 4 eV leading to LIDTs exceeding those of the Ag analogs, while their NLO efficiencies were slightly lower. For example, the band gap of $LiGaS_2$ is 3.65 eV, which is significantly larger than that of

[a]State Key Laboratory of Structural Chemistry, Fujian Institute of Research on the Structure of Matter, Chinese Academy of Sciences, Fuzhou, Fujian 350002, P. R. China. E-mail: gcguo@fjirsm.ac.cn; xmjiang@fjirsm.ac.cn

[b]School of Chemistry and Chemical Engineering, Yangtze Normal University, P. R. China

† Electronic supplementary information (ESI) available. CCDC 1842640, 1842642, 1842643 and 1842644. For ESI and crystallographic data in CIF or other electronic format see DOI: 10.1039/c8sc01210e

AGS (2.62 eV);[26] nevertheless, the SHG coefficient of $LiGaS_2$ is approximately a quarter of that of AGS.[27] The other method involves combining two or more NLO-active motifs such as GaQ_4, InQ_4, GeQ_4, or SiQ_4 (Q = S, Se) tetrahedra in a single IR NLO chalcogenide compound to modulate the LIDT and NLO efficiency.[28–44] The combination of different NLO-active motifs can optimize the NLO efficiency and LIDT effectively. For example, by incorporating GeS_2 into $AgGaS_2$, quaternary $AgGaGeS_4$ was developed with an improved LIDT, which makes it a promising alternative to the widely used AGS.[45–47] Additionally, a series of Li-containing quaternary compounds have been reported, including $Li_2Ga_2GeS_6$, $LiGaGe_2Se_6$, $Li_2In_2GeSe_6$, and $Li_2In_2SiSe_6$; the combination of different microscopic NLO-active units, namely, GaQ_4, InQ_4, GeQ_4 and SiQ_4, in these compounds strengthens their nonlinear susceptibilities compared with those of the corresponding ternary compounds.[21,48,49] Although there have been many attempts using these two main methods, excellent IR NLO materials with both a high LIDT and high NLO efficiency are rare.

Theoretically, SHG is a two-photon process, and the value for NLO efficiency is determined by the optical transition matrix elements, which strongly depend on the band gap of an IR NLO material.[50] Normally, a small band gap can easily result in a strong optical transition and is therefore beneficial for a large NLO efficiency. Compared with SHG, laser damage on NLO crystals is a highly complicated process that involves pitting, erosion, melting, delamination, fracture, and discoloration.[51] The mechanisms of the laser damage process can be mainly categorized into thermal processes and dielectric processes. For NLO crystals with high laser transparency and few defects for optical absorption, the dielectric process mechanism is applied, and the dielectric LIDT is proportional to the atomic density/$(n^2 - 1)$, where n is refractivity and has large values for materials with narrow band gaps. Therefore, narrow band gaps simultaneously lead to large NLO efficiencies and low LIDTs. This result is also the reason for the so-called incompatibility between a large NLO efficiency and a high LIDT in some NLO compound systems, such as the well-known oxides and the IA–IIIA–VIA_2 type of IR NLO material.[7]

However, for many practical mid-IR NLO materials, intrinsic and defect-induced optical absorptions are non-negligible, which may lead to a temperature increase when the laser beam is incident on the surface of an NLO crystal, thereby resulting in thermal expansion, strain, distortion, cracking, catastrophic shattering and so on. Under these conditions, the thermal process mechanism can be applied;[51] the corresponding thermal LIDTs scale proportionally to $C\kappa S/\alpha\beta$, where C is the heat capacity of the material, for which values can seem close together for any solids with similar atomic densities above room temperature, κ is the thermal conductivity, S is the damaging stress and is positively correlated with the Young's modulus and shear modulus of the material, β is the expansion coefficient and α is the absorption coefficient. These results show that the LIDT can be enhanced by reducing the thermal effects, *i.e.*, by increasing the thermal conductivity and damaging stress, and decreasing the expansion and absorption coefficients of IR NLO materials.

The intrinsic physical parameters of NLO crystals, the thermal conductivity, damaging stress, and absorption coefficients, strongly depend on the microscopic structural features of crystals, such as the number and size of localized absorbing defects and impurities.[52–54] Nevertheless, the expansion coefficient of a particular type of NLO crystal does not change significantly under different crystal growing conditions. Therefore, from the perspective of the crystal structure design of mid-IR NLO materials, the parameter of expansion coefficient may be modulated in a relatively easy manner to enhance the LIDT. The expansion coefficient of a compound depends on the expansion coefficients (dR/dT) of all its chemical bonds, which can be evaluated through $dR/dT = 1.35\ k/G$ based on the bond-valence theory,[55] where k is the Boltzmann constant and G is the force constant of the chemical bonds. Normally, for the same type of chemical bond, G is larger for shorter bond lengths. However, for the same types of center and coordinated ion, according to the bond-valence-sum rule, center ions that have fewer coordinated atoms are likely to have shorter bond lengths and larger force constants. In such circumstances, relatively smaller thermal expansion coefficients and higher LIDT values can be predicted.

For the case in which a thermal LIDT dominates the laser-induced damage process in the practical application of mid-IR NLO materials, the NLO efficiency and LIDT are relatively independent of each other, and almost no incompatibility exists between them. We propose a new strategy for designing IR NLO materials by narrowing the band gap for a large NLO efficiency and reducing the thermal effect for a high laser-induced damage threshold. This approach is effective in achieving high NLO efficiency and a high LIDT concurrently.

Recently, metal chalcogenides have been found to be highly attractive for the exploration of new mid-IR NLO materials. Some alkali-metal-containing quaternary chalcogenides were reported to exhibit large NLO efficiencies, such as $K_4GeP_4Se_{12}$,[56] $Na_2Ge_2Se_5$,[57] K_3TaAsS_{11},[10] and $CsZrPSe_6$,[58] which possess NLO coefficients of 14.02, 12.01, 9.91, and 9.92 times that of AGS, respectively. Highly electropositive alkali metals in these chalcogenides usually play the role of dimensional reduction agents to reduce the coordinated atoms of the host chalcogenide frameworks. Based on the preceding analysis, besides having high NLO efficiencies, alkali-metal-containing chalcogenides may exhibit high LIDTs due to the strengthening of their force constants and the reduction in the thermal expansion coefficients of the metal–chalcogen bonds.

To verify our new strategy, we synthesized four new compounds in the alkali metal sodium-containing chalcogenides, namely, $Na_2Ga_2GeSSe_5$ (**1**), $Na_2Ga_2GeSe_6$ (**2**), $Na_2Ga_2SnSSe_5$ (**3**), and $Na_2Ga_2SnSe_6$ (**4**). All these materials exhibit phase-matching behavior with a large NLO efficiency of 1.6–3.9 × that of AGS. Their band gaps are obviously narrower than those of AGS, which should result in relatively smaller LIDTs based on the conventional view. However, the four compounds exhibit extremely large LIDTs of 8.5–13.3 × that of AGS, which can be attributed to their small thermal expansion anisotropy compared to that of AGS. In the following section, we report the synthesis and characterization and the optical and thermal

properties of these compounds. Theoretical calculation of the electronic band structures and NLO efficiencies was also conducted for these compounds.

Experimental section

Synthesis

The following chemicals were used in this study: Na (99.7%), Ga (99.99%), Ge (99.99%), Sn (99.9%), S (99.5%), and Se (99.9%). All of these chemicals were from Aladdin Chemistry Co. Ltd. and were used as received without further purification. The Na_2S and Na_2Se starting materials were prepared through stoichiometric reaction of Na and S or Se in liquid ammonia.[30] For the synthesis of the target compounds, a stoichiometric mixture of the starting materials Na_2S, Ga, Ge (Sn), and Se in a molar ratio of 1 : 2 : 1 : 5 for **1** and **3**, and Na_2Se, Ga, Ge (Sn), and Se in a molar ratio of 1 : 2 : 1 : 6 for **2** and **4**, were loaded into a graphite crucible and placed in quartz tubes. The tubes were flame-sealed under vacuum ($\sim 10^{-4}$ Torr) and then placed in a temperature-controlled muffle furnace, heated from room temperature to 800 °C in 40 h, kept at that temperature for 96 h, and then cooled to room temperature at 4 °C per hour. The products were washed with degassed DMF and dried with ethanol. Yellow crystals of **1** and **2**, orange crystals of **3**, and red crystals of **4**, with the respective yields of 60%, 60%, 70%, and 50% based on Ga for **1–4**, were obtained. All the compounds were stable in air and water.

Single-crystal structure determination

Block single crystals of **1–4** were selected for single-crystal diffraction. Diffraction data were collected using graphite monochromated Mo Kα radiation ($\lambda = 0.71073$ Å) on a Rigaku Pilatus CCD diffractometer at 293 K. The intensity data sets were collected with a ω-scan technique and reduced using CrystalClear software.[59]

The structures of **1–4** were solved by direct methods and refined using the full-matrix least-squares method on F^2 with anisotropic thermal parameters for all the atoms. All the calculations were performed with a SHELXL package of crystallographic software.[60] The formulas collectively consider the crystallographically refined compositions and requirements of charge neutrality. The Addsym/Platon program was used to check the final structures for additional symmetry, and no other missed or higher symmetry element was found.[61] The crystal data and structural refinement information for **1–4** are summarized in Table 1. The atomic coordinates and equivalent isotropic displacement parameters are listed in Table S1.† Selected bond distances are reported in Table S2.†

Powder X-ray diffraction

Powder X-ray diffraction (PXRD) measurements were performed on a Rigaku MiniFlex II diffractometer using Cu Kα radiation in reflection mode at room temperature with a step size of 0.02° in the range $2\theta = 5$–65°. The experimental and simulated PXRD patterns of **1–4** are shown in Fig. S2,† indicating the purity of the as-synthesized samples, despite the possible existence of a tiny amount of $NaGa_3Se_5$ in phase **2**.

Energy-dispersive X-ray spectroscopy analysis

Semiquantitative microprobe element analyses of crystals of the four compounds were performed with a field emission scanning electron microscope (FESEM, JSM6700F) equipped with an energy-dispersive X-ray spectroscopy instrument (EDX, Oxford INCA). The empirical formulas $Na_{2.3}Ga_{2.1}Ge_{1.0}S_{0.8}Se_{5.1}$ for **1**, $Na_{1.9}Ga_{2.3}Ge_{1.0}Se_{5.8}$ for **2**, $Na_{2.2}Ga_{2.3}Sn_{1.0}S_{1.0}Se_{5.1}$ for **3**, and $Na_{1.8}Ga_{2.0}Sn_{1.0}Se_{6.1}$ for **4** were obtained, and no other element was detected (Fig. S1†), which was consistent with the results determined from single-crystal XRD.

SHG measurements

The SHG measurements of **1–4** were taken using a modified Kurtz–Perry powder technique with 1910 nm laser radiation.[62] Microcrystalline powder samples were ground and sieved into several distinct particle size ranges (30–50, 50–75, 75–100, 100–125, 125–150, and 150–200 μm) for the SHG phase-matching measurements. AGS crystals with similar particle sizes were used as references. During measurement, all of the samples were pressed between two glass microscope cover slides and secured in the 1 mm-thick plastic holders. After the mixed signals passed through the monochromator, the doubled frequency signals (955 nm) were detected by an Andor DU420A-BR-DD CCD.

Powder LIDT measurements

The powder LIDTs of **1–4** and the reference AGS were evaluated using the single-pulse measurement method using a focused high-power 1064 nm laser beam with a pulse width (τ_p) of 10 ns and a repetition rate of 1 Hz.[63] The measurements were conducted by gradually increasing the laser power until a damaged spot on the samples was observed under the microscope after irradiation. The Nova II sensor with a PE50-DIF-C energy sensor and a vernier caliper were respectively used to measure the power of the laser beam and to identify the damaged spots.

Thermal analyses

The thermal properties of **1–4** were investigated using differential scanning calorimetry (DSC) analysis using a Netzsch STA 449C thermal analyzer under a nitrogen atmosphere. Each sample of approximately 10 mg was placed in a sealed silica tube evacuated to 10^{-4} Torr, heated to 900 °C at 10 °C min^{-1} and cooled to 30 °C at 10 °C min^{-1}.

Electronic structure calculations

Electronic band structures and densities of states (DOS) of **1–4** were calculated using the structure models obtained directly from single-crystal XRD analysis, which were calculated based on density functional theory (DFT) with CASTEP code provided by a Materials Studio package.[64,65] The electrons in Na: $2s^2 2p^6 3s^1$, Ga: $3d^{10} 4s^2 4p^1$, Ge: $4s^2 4p^2$, Sn: $5s^2 5p^2$, S: $3s^2 3p^4$ and Se: $4s^2 4p^4$ were treated as valence electrons. The plane-wave

Table 1 Crystal data and structure refinement parameters for **1–4**

	1	**2**	**3**	**4**
Chemical formula	$Na_2Ga_2GeSSe_5$	$Na_2Ga_2GeSe_6$	$Na_2Ga_2SnSSe_5$	$Na_2Ga_2SnSe_6$
Formula weight	684.87	731.77	730.97	777.87
Crystal size (mm^3)	0.117 × 0.115 × 0.106	0.110 × 0.105 × 0.102	0.117 × 0.083 × 0.066	0.071 × 0.063 × 0.046
Crystal system	Orthorhombic			
Space group	*Fdd*2			
a (Å)	12.987(10)	12.985(4)	13.264(4)	13.329(3)
b (Å)	23.653(17)	23.880(8)	23.936(7)	24.291(7)
c (Å)	7.519(5)	7.585(3)	7.514(2)	7.621(2)
V ($Å^3$)	2310(3)	2352.0(14)	2385.6(12)	2467.5(11)
Z	8	8	8	8
D_{calcd} (g cm^{-3})	3.939	4.133	4.070	4.188
μ (mm^{-1})	23.170	25.671	22.007	24.058
θ Range (°)	3.25–25.46	3.23–25.46	3.40–25.46	3.19–25.47
GOF on F^2	1.049	0.977	1.114	1.101
$R_1{}^a$ [$I > 2\sigma(I)$]	0.0375	0.0238	0.0257	0.0209
$wR_2{}^b$ [$I > 2\sigma(I)$]	0.0990	0.0486	0.0661	0.0549
$R_1{}^a$ (all data)	0.0389	0.0285	0.0270	0.0218
$wR_2{}^b$ (all data)	0.1009	0.0496	0.0668	0.0551
Flack parameter x	0.00	0.00	0.00	0.00
$\Delta\rho_{max}/\Delta\rho_{min}$ (e $Å^{-3}$)	1.288/−0.991	0.538/−0.986	0.662/−0.768	0.852/−0.528

cutoff energy was set to 800 eV for **1–4**. Moreover, the numerical integration of the Brillouin zone was performed using 2 × 1 × 3 Monkhorst–Pack k-point meshes for all the compounds. The Fermi level ($E_f = 0$ eV) was selected as a reference.

Theoretical calculations on the optical properties regarding the complex dielectric function $\varepsilon(\omega) = \varepsilon_1(\omega) + i\varepsilon_2(\omega)$ were carried out as follows:[66,67]

$$\varepsilon_2(\omega) = \frac{2e^2\pi}{\Omega\varepsilon_0}\sum_{K,V,C}\left|<\Psi_K^C|\hat{u}\cdot r|\Psi_K^V>\right|^2\delta\left(E_K^C - E_K^V - E\right), \quad (1)$$

where $\delta(E_K^C - E_K^V - E)$ indicates the energy difference between the conduction and valence bands at the k point with absorption of energy E, $\hat{u}$ denotes the polarization of the incident electric field, Ω is the volume of the primitive cell, e is the electric charge, Ψ_K^C and Ψ_K^V are the vectors defining the conduction and valence band wave functions at k, respectively, and $\varepsilon_1(\omega)$ can be obtained using the dispersion relationship of Kramers–Kronig as follows:

$$\varepsilon_1(\omega) = 1 + \frac{2}{\pi}P\int_0^\infty \frac{\omega'\varepsilon_2(\omega')}{\omega'^2 - \omega^2}d\omega'. \quad (2)$$

The P before the integral indicates the principal value. The first-order nonresonant susceptibility at the low-frequency region is given by $\chi^{(1)}(\omega) = \varepsilon_1(\omega) - 1$, and the second-order susceptibilities were calculated using the anharmonic oscillator model.[50]

Results and discussion

Crystal structure

Compounds **1–4** are isostructural and crystallize in the NCS space group *Fdd*2 in the orthorhombic system with the unit cell parameters a = 12.432(4)–13.329(3) Å, b = 22.584(7)–24.291(7) Å, c = 7.239(2)–7.261(2) Å, and Z = 8. In the asymmetric unit, two crystallographically independent positions are observed for Ga, Ge, or mixed Ga/Sn atoms; three positions for fully occupied S, Se, or mixed S/Se atoms; and one position for Na.

In compound **1**, the 3D framework consists of two different building blocks, namely, 1D infinite $_\infty{}^1[Ga(S/Se)Se_2)]^{3-}$ chains (pink tetrahedral chains in Fig. 1a) and isolated $[Ge(S/Se)_2Se_2]^{4-}$ tetrahedra (green tetrahedra in Fig. 1a). Each Ga atom is coordinated by one mixed S/Se and three Se atoms forming the $[Ga(S/Se)Se_3)]^{5-}$ tetrahedra with Ga–S/Se distances ranging from 2.359 Å to 2.406 Å, which then connect with each other by sharing common S/Se atoms to form infinite linear $_\infty{}^1[Ga(S/Se)Se_2)]^{3-}$ chains. Similar to the Ga atoms, each Ge atom is tetrahedrally coordinated by two mixed S/Se and two Se atoms to form the $[Ge(S/Se)_2Se_2]^{4-}$ tetrahedra with Ge–S/Se distances ranging from 2.352 Å to 2.374 Å. These two different building blocks, namely, the infinite $_\infty{}^1[Ga(S/Se)Se_2)]^{3-}$ chains and the isolated $[Ge(S/Se)_2Se_2]^{4-}$ tetrahedra, are assembled to form the 3D anionic $(Ga_2GeSSe_5)^{2-}$ framework of **1** (Fig. 1b). Two groups of $_\infty{}^1[Ga(S/Se)Se_2)]^{3-}$ chains along the $a + c$ and $a - c$ directions intersect each other with $[Ge(S/Se)_2Se_2]^{4-}$ tetrahedra acting as the connections between them and forming tunnels along the c direction, which are embedded with the Na^+ counter cations.

All positions in **2** are fully occupied. In compound **3**, besides the S/Se mixing, the Ga and Sn positions are mixed with the molar ratio 2 : 1. The Sn positions in **4**, similar to the Ge positions in **1**, are mixed with Ga with half occupancy. The mixed occupancy of the S/Se and Ga/Sn positions is determined by the structural refinements that consider charge balance. The Ga–S(Se), Ge–S(Se), (Ga/Sn)–S, and Na–S(Se) bond lengths in **1–4** (Table S2†) are close to those in $BaGa_4S_7$,[25] $BaGa_2GeS_6$,[36] $Ba_2Ga_8GeS_{16}$,[41] $PbGa_2GeSe_6$,[18] $Na_4MgGeSe_6$,[68] $Ba_5Ga_2Se_8$,[69] $KCd_4Ga_5Se_{12}$,[70] $Na_3Mo_{15}Se_{19}$,[71] and $Na_4Sn_3S_8$.[72]

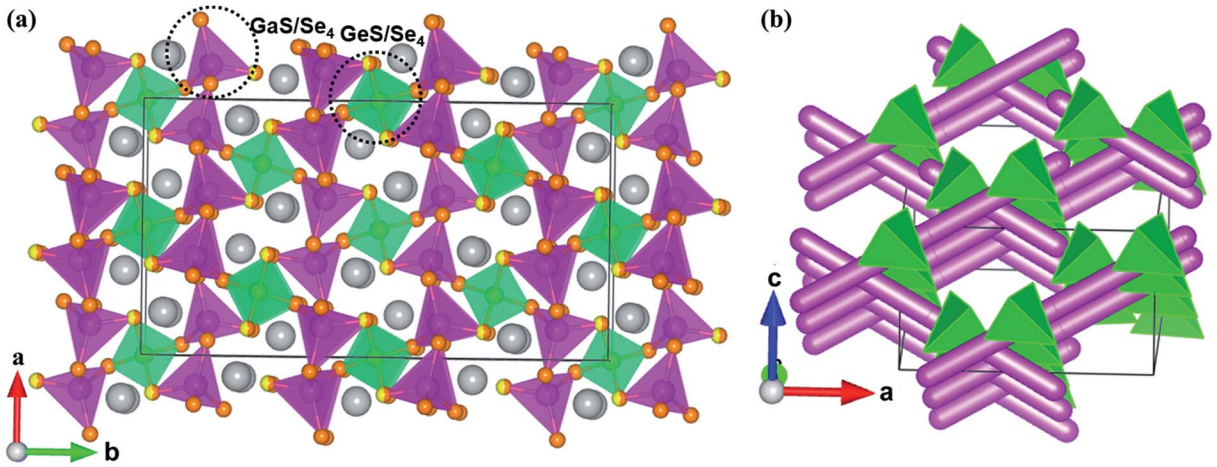

Fig. 1 (a) The 3-D structure of **1** viewed down the *c* direction. Grey atoms: Na, pink tetrahedra: $[Ga(S/Se)Se_3)]^{5-}$, green tetrahedra: $[Ge(S/Se)_2Se_2]^{4-}$; yellow/orange atoms: S/Se atoms. (b) The infinite $_\infty{}^1[Ga(S/Se)Se_2)]^{3-}$ chains represented by pink columns and isolated $[Ge(S/Se)_2Se_2]^{4-}$ connections (green tetrahedra) in the unit cell of **1**. The Na^+ cations are left out for clarity.

Interestingly, modifying the chalcogen ratio and mutual replacement of Ga, Ge, and Sn atoms does not lead to structural changes in the $Na_2Ga_2MQ_6$ (M = Ge, Sn; Q = S, Se) system. Structure retention such as this is important when conducting chalcogen or metal doping to optimize the physical performance of these materials, similar to the case with nonlinear optical materials.[73]

NLO properties

The SHG of **1–4** was investigated using a 1910 nm laser and AGS as the reference. The SHG signals of **1–4** as a function of particle size are shown in Fig. 2. Their SHG intensities increase with the growth in particle size. These results are consistent with type-I phase-matching behavior, which is important in practical applications. Remarkably, the SHG intensities of **1–4** are about 2.3, 1.6, 3.9, and 2.1 times that of commercial AGS with the particle size from 75–100 μm (Fig. 2b). Generally, the SHG signal intensity measured by the Kurtz–Perry powder method is proportional to the square of the second-order NLO coefficient d_{eff}, and the reported d_{eff} of AGS is 12.5 pm V^{-1}.[26] Thus, the derived d_{eff} values for **1–4** are 18.95, 15.81, 24.68, and 18.11 pm V^{-1}.

Interestingly, compound **3** $Na_2Ga_2SnSSe_5$ has the highest SHG intensity among these compounds, whereas compound **2** has the lowest. This result is reasonable according to the structural analysis. Both S/Se and Ga/Sn occupancy disorders are observed in **3**, which can lead to structural distortion and the enhancement of noncentrality and SHG intensity, compared to that in the corresponding perfect structure. Moreover, the cation size effect may also have an effect on the formation of these compounds and ultimately their NLO properties.[74,75]

In contrast, no mixing position can be observed in **2**, and no additional SHG enhancement from the structural distortion is present. In the case of **1** and **4**, either S/Se (**1**) or Ga/Sn (**4**) is present in their structures, and their SHG intensities are between those of **2** and **3**. Given the structure retention of the $Na_2Ga_2MQ_6$ (M = Ge, Sn; Q = S, Se) system under chalcogen and

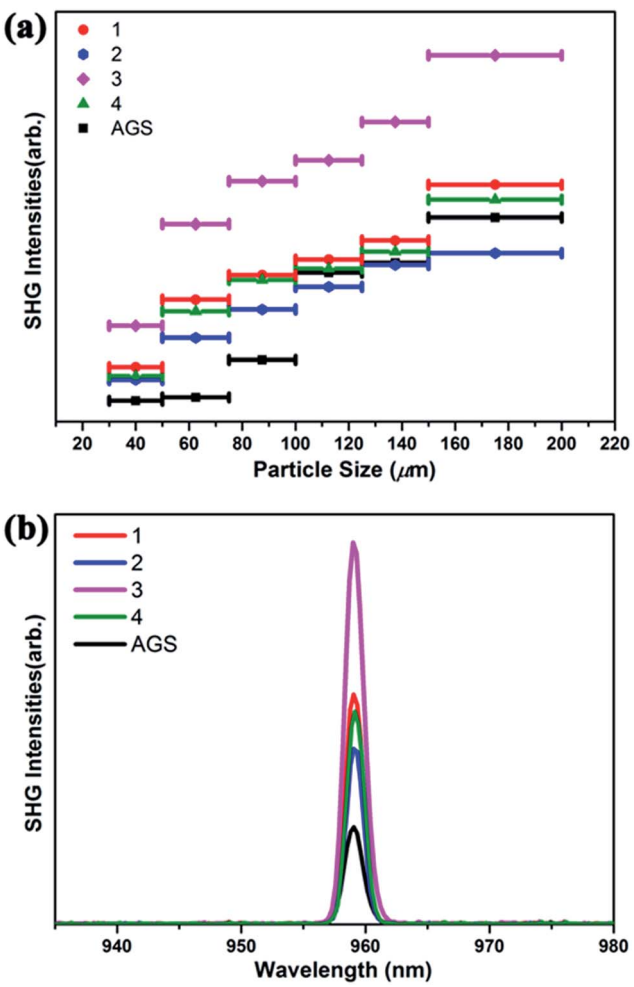

Fig. 2 (a) Phase-matching curves of **1–4** and the reference AGS. (b) SHG intensities of **1–4** with AGS as the reference in the particle size range 75–100 μm.

metal variation, new compounds with SHG intensity even higher than that of **3** could be obtained by chalcogen and metal variation.

The IR transmission spectra show that compounds **1–4** have no obvious intrinsic absorption from chemical bonds in a broad spectral range from 0.25 to 25 μm (Fig. S3†), indicating that compounds **1–4** may be good candidates for a variety of NLO applications in the mid- and far-IR regions. The optical diffuse reflectance spectra indicate optical band gaps (E_g) of 1.56, 1.61, 1.63 and 1.73 eV for **1–4** (Fig. S4†), which are significantly smaller than that of AGS (2.65 eV).[1] The NLO efficiency is positively associated with the band gap, and the band gaps of **1–4** being narrower than that of AGS is consistent with their NLO efficiencies being larger than that of AGS. The band-gap order $E_g(\mathbf{1}) < E_g(\mathbf{2}) < E_g(\mathbf{3}) < E_g(\mathbf{4})$ is not in accordance with the opposite of the NLO efficiency order $d_{eff}(\mathbf{2}) < d_{eff}(\mathbf{4}) < d_{eff}(\mathbf{1}) < d_{eff}(\mathbf{3})$, which can be attributed to the role of structure distortion induced by atom mixing. Overall, narrowing the band gap of an NLO material is an effective way to achieve a large NLO efficiency.

Powder LIDTs

The powder LIDTs of **1–4** and the benchmark AGS measured by the single pulse method are summarized in Table 2. For measurement, small spot areas with the sizes 0.1590, 0.1662, 0.2463 and 0.1963 cm^2 were selected for **1–4**, respectively. The measured damage energies of **1–4** (20.07–27.99 mJ) were much higher than that of AGS (11.02 mJ). The derived powder LIDTs of **1–4** were 9.9, 13.3, 8.5, and 10.1 times that of AGS, supporting their potential for high-power applications. In this study, the experimental LIDT of the benchmark AGS was 1.27 MW per cm^{-2}, which is close to reported values.[18] According to the conventional view of the incompatibility between a large NLO efficiency and a high LIDT for NLO materials, compounds **1–4** with band gaps significantly narrower than that of AGS should have a smaller LIDT.

However, the experimental LIDT values for **1–4** are much higher than that of AGS, and there should be other factors that dominate the LIDT of **1–4**, rather than the band gap, although the LIDT order LIDT (**3**) < LIDT (**1**) < LIDT (**4**) < LIDT (**2**) is in accordance with the opposite of the NLO efficiency order $d_{eff}(\mathbf{2}) < d_{eff}(\mathbf{4}) < d_{eff}(\mathbf{1}) < d_{eff}(\mathbf{3})$. This issue is discussed in the following section.

Thermal properties

Thermal effects are non-negligible in the practical application of mid-IR NLO materials; the large temperature increase caused by optical absorptions leads to thermal expansion, strain, distortion, cracking, catastrophic shattering, and damage of crystals.[51] The thermal expansion anisotropy (TEA, δ) of NLO materials is identified as one of the most important intrinsic parameters to influence the ultimate experimentally derived LIDTs. NLO materials with smaller TEAs tend to sustain a larger thermal shock under laser irradiation and exhibit higher LIDTs. To study the TEA of **1–4** and the reference AGS, the temperature dependence of the lattice parameters was measured using an X-ray diffractometer from 300 K to 500 K with a step of ~20 K (Fig. S6†). The thermal expansion coefficients (TECs, $\alpha_L = R_0^{-1}[dR(T)/dT]$, where R_0 is the value at $T = 0$ K) of the lattice parameters (a, b and c are the axis lengths) of **1–4** were derived. The TEA (δ) values, defined as the ratio of the maximum and minimum of the TEC, are 1.59, 1.49, 2.01 and 1.51 for **1–4** (Table 3). The TEC and TEA of AGS have been measured in our previous work[76] and are close to other reported values.[77]

The measured TEA order $\delta(\text{AGS}) > \delta(\mathbf{3}) > \delta(\mathbf{1}) > \delta(\mathbf{4}) > \delta(\mathbf{2})$ is in accordance with the experimental LIDTs, which have the opposite order. According to the structural analysis of the four compounds, atom mixing occurs in all the structures except **2**, where the structural defects are indispensable, as are the defect-induced optical absorptions during measurement. The TEA is proposed to be the dominant factor in the LIDTs of the $Na_2Ga_2MQ_6$ (M = Ge, Sn; Q = S, Se) system, as supported by the experimental results. Reducing the thermal effect, especially by decreasing the thermal expansion anisotropy of an NLO material, is reasonable for achieving a high LIDT. The TEA and LIDT values of some typical IR NLO crystals, $LiInS_2$, $ZnGeP_2$, GaSe and $AgGaSe_2$ have been listed in Table S3.† The TEAs of $ZnGeP_2$ and GaSe are close to each other, resulting in them having similar LIDTs. The TEA of $LiInS_2$ is much larger than that of AGS. However, its LIDT is also much larger than that of AGS, which can be ascribed to the shorter pulse width used for the LIDT measurement of $LiInS_2$.

The DSC results in Fig. S5† show that compounds **1–4** undergo congruent melting upon heating and crystallization upon cooling with relatively low melting temperatures (606, 571, 659, and 689 °C for **1–4**). In comparison, the melting points of the known IR NLO materials, such as AGS (998 °C), $LiGaS_2$ (1050 °C), $LiGaSe_2$ (915 °C), $BaGa_4S_7$ (1090 °C), and $BaGa_4Se_7$ (968 °C)[40] are significantly higher. These results reveal that large crystals of **1–4** can be grown using the Bridgman method at lower temperatures.

Theoretical calculations

The theoretical band gaps of **1–4** were calculated to be 2.01, 2.02, 2.00, and 1.95 eV, (Fig. S7†). Compared with the

Table 2 LIDTs of **1–4**

Compound	Damage energy (mJ)	Spot area (cm^2)	Damage threshold [MW cm^{-2}]
1	20.07	0.1590	12.62
2	27.99	0.1662	16.84
3	26.59	0.2463	10.79
4	25.19	0.1963	12.82
AGS	11.02	0.8659	1.27

Table 3 Thermal expansion coefficients α_L ($\times 10^{-5}$ K^{-1}) of a, b and c axis lengths and the thermal expansion anisotropy of **1–4** and the reference AGS

	1	**2**	**3**	**4**	AGS
a	5.58	5.86	−5.46	3.68	3.08
b	−5.54	6.85	−2.71	−4.09	3.08
c	−8.81	−8.75	2.99	5.52	−9.158
δ	1.59	1.49	2.01	1.51	2.97

experimental results, the calculated band gaps of **1–4** have certain deviations due to the limitations of the DFT method in semiconductors and insulators.[78,79] As observed from the partial DOS presented in Fig. S8,† for all four compounds, the valence band close to the Fermi level originates predominantly from Se-4p and S-3p states for **1** and **3** and Se-4p for **2** and **4**. The conduction bands (CB) of **1–4** close to the bottom of the CB are mostly composed of Ga-4p, Ge-4p and Se-4p states in **1**, Ge-4p and Se-4s states in **2**, and Sn-5p and Se-4s states in **3** and **4**. Therefore, their optical absorptions can be mainly attributed to charge transfer from the Se-4p (S-3p) states to the Sn-5p (Ga-4p, Ge-4p) and Se-4p (Se-4s) states, and the electronic structure around the band edges is mainly derived from the (Sn/Ga/Ge)(S/Se)$_4$ tetrahedra units, which provide the dominant states in the optical matrix elements describing the virtual excitations of the SHG effect in **1–4**. The strongly isolated s and p orbitals of the Na^+ cations are localized far from the band gaps and have a negligible influence on the SHG effect.

To obtain a profound understanding of the NLO properties of **1–4**, theoretical calculations of the SHG coefficients were performed. The real (ε_1) and imaginary (ε_2) parts of the optical dielectric constants along the x, y and z directions are shown in Fig. S9 and S10.† The curves of ${\varepsilon_2}^{ave}$, defined as $(\varepsilon_x + \varepsilon_y + \varepsilon_z)/3$, reveal that the strongest absorptions of **1** are at 5.72, of **2** are at 5.54, of **3** are at 8.54, and of **4** are at 8.74 eV, which can be mainly assigned to the electronic interband transitions according to the DOS analysis. Owing to the NCS point group of *mm*2, compounds **1–4** have three independent non-zero SHG tensors d_{113}, d_{223}, and d_{333} under the restriction of Kleinman symmetry. The calculated energy dependence of the SHG tensors of **1–4** is shown in Fig. 3, at the wavelength 1910 nm (0.6492 eV). The d_{113}, d_{223}, and d_{333} values are 18.72, 19.22 and 19.09 pm V^{-1} for **1**; 13.89, 13.39 and 13.84 pm V^{-1} for **2**; 23.69, 22.10 and 22.28 pm V^{-1} for **3**; and 17.06, 16.83 and 16.21 pm V^{-1} for **4**. The calculated average SHG coefficients d_{cal} defined as the arithmetic mean of all the SHG tensors which in descending order are d_{cal}(**3**, 22.69 pm V^{-1}) > d_{cal}(**1**, 19.01 pm V^{-1}) > d_{cal}(**4**, 16.70 pm V^{-1}) > d_{cal}(**2**, 13.71 pm V^{-1}) are consistent with the experimental results.

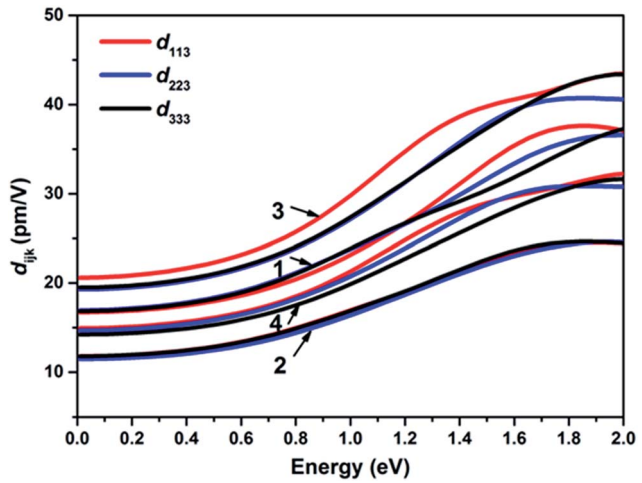

Fig. 3 The calculated frequency-dependent SHG coefficients for **1–4**.

Conclusions

A new strategy to circumvent the incompatibility between large NLO efficiencies and high LIDTs in mid-infrared NLO materials, namely, narrowing the band gap for a large NLO efficiency and reducing the thermal effect for a high LIDT, is proposed in this study. To support this proposal, a series of isostructural chalcogenides with different tetrahedral center cations, $Na_2Ga_2MQ_6$ (M = Ge, Sn; Q = S, Se), were successfully synthesized using the solid-state method. The 3D structures of these chalcogenides were assembled in 1D infinite $_\infty{}^1[Ga(Sn)Q_3]^{3-}$ tetrahedral chains and $[MQ_4]^{4-}$ tetrahedral connections. All of them exhibit large SHG responses of approximately 1.6–3.9 × that of AGS with phase-matching ability, which result from their relatively small band gaps (1.56–1.73 eV) compared with that of AGS (2.65 eV). They also exhibit outstanding LIDTs of 8.5–13.3 × that of AGS for potential high-power applications, which is contrary to the conventional view on band gaps. However, the measured thermal expansion anisotropy order of these compounds is in agreement with their experimental LIDTs, which have the opposite order, indicating that the thermal expansion anisotropy is one of the main thermal parameters to influence the LIDTs of IR NLO materials and a high LIDT can be achieved by reducing the thermal effect. The results of this study shed light on the search for practical IR NLO materials with excellent performance which are not restricted by the NLO–LIDT incompatibility.

Conflicts of interest

There are no conflicts to declare.

Acknowledgements

This work was financially supported by the NSF of China (21701176), the National Postdoctoral Program for Innovative Talents (BX201600163), the China Postdoctoral Science Foundation (2016M600510), the National Key Laboratory Development Fund (20180026) and the NSF of Fujian Province (2018J05034).

Notes and references

1 L. Kang, M. Zhou, J. Yao, Z. Lin, Y. Wu and C. Chen, *J. Am. Chem. Soc.*, 2015, **137**, 13049.
2 H. Zhang, M. Zhang, S. Pan, X. Dong, Z. Yang, X. Hou, Z. Wang, K. B. Chang and K. R. Poeppelmeier, *J. Am. Chem. Soc.*, 2015, **137**, 8360.
3 H. Yu, J. Young, H. Wu, W. Zhang, J. M. Rondinelli and P. S. Halasyamani, *J. Am. Chem. Soc.*, 2016, **138**, 4984.
4 I. Chung and M. G. Kanatzidis, *Chem. Mater.*, 2014, **26**, 849.
5 C. Chen, *Sci. Sin., Ser. B*, 1985, **28**, 235.
6 C. Chen, Y. Wu, A. Jiang, B. Wu, G. You, R. Li and S. Lin, *J. Opt. Soc. Am. B*, 1989, **6**, 616.

7 V. G. Dmitriev, G. G. Gurzadyan and D. N. Nikogosyan, *Handbook of nonlinear optical crystals*, Springer-Verlag, New York, 1999.
8 C. Chen, Y. Wang, B. Wu, K. Wu, W. Zeng and L. Yu, *Nature*, 1995, **373**, 322.
9 T. A. Driscoll, P. E. Perkins, H. J. Hoffman and R. E. Stone, *J. Opt. Soc. Am. B*, 1986, **3**, 683.
10 T. K. Bera, J. I. Jang, J. B. Ketterson and M. G. Kanatzidis, *J. Am. Chem. Soc.*, 2008, **131**, 75.
11 I. Chung and M. G. Kanatzidis, *Chem. Mater.*, 2013, **26**, 849.
12 F. Liang, L. Kang, Z. Lin and Y. Wu, *Cryst. Growth Des.*, 2017, **17**, 2254.
13 A. Harasaki and K. Kato, *Jpn. J. Appl. Phys.*, 1997, **36**, 700.
14 A. Jayaraman, V. Narayanamurti, H. Kasper, M. Chin and R. Maines, *Phys. Rev. B: Solid State*, 1976, **14**, 3516.
15 G. Catella, L. Shiozawa, J. Hietanen, R. Eckardt, R. Route, R. Feigelson, D. Cooper and C. Marquardt, *Appl. Opt.*, 1993, **32**, 3948.
16 M. C. Ohmer and R. Pandey, *MRS Bull.*, 1998, **23**, 16–22.
17 G. Boyd, E. Buehler and F. Storz, *Appl. Phys. Lett.*, 1971, **18**, 301.
18 Z. Z. Luo, C. S. Lin, H. H. Cui, W. L. Zhang, H. Zhang, H. Chen, Z. Z. He and W. D. Cheng, *Chem. Mater.*, 2015, **27**, 914.
19 G. Li, K. Wu, Q. Liu, Z. Yang and S. Pan, *J. Am. Chem. Soc.*, 2016, **138**, 7422.
20 K. Wu, Z. Yang and S. Pan, *Chem. Mater.*, 2016, **28**, 2795.
21 A. P. Yelisseyev, L. I. Isaenko, P. Krinitsin, F. Liang, A. A. Goloshumova, D. Y. Naumov and Z. Lin, *Inorg. Chem.*, 2016, **55**, 8672.
22 S. Fossier, S. Salaün, J. Mangin, O. Bidault, I. Thénot, J.-J. Zondy, W. Chen, F. Rotermund, V. Petrov, P. Petrov, J. Henningsen, A. Yelisseyev, L. Isaenko, S. Lobanov, O. Balachninaite, G. Slekys and V. Sirutkaitis, *J. Opt. Soc. Am. B*, 2004, **21**, 1981.
23 V. Petrov, J. J. Zondy, O. Bidault, L. Isaenko, V. Vedenyapin, A. Yelisseyev, W. Chen, A. Tyazhev, S. Lobanov and G. Marchev, *J. Opt. Soc. Am. B*, 2010, **27**, 1902.
24 L. Isaenko, A. Yelisseyev, S. Lobanov, P. Krinitsin, V. Petrov and J. J. Zondy, *J. Non-Cryst. Solids*, 2006, **352**, 2439.
25 X. Lin, G. Zhang and N. Ye, *Cryst. Growth Des.*, 2008, **9**, 1186.
26 J. J. Zondy, D. Touahri and O. Acef, *J. Opt. Soc. Am. B*, 1997, **14**, 2481.
27 V. Petrov, A. Yelisseyev, L. Isaenko, S. Lobanov, A. Titov and J. J. Zondy, *Appl. Phys. B: Lasers Opt.*, 2004, **78**, 543.
28 G. A. Marking, J. A. Hanko and M. G. Kanatzidis, *Chem. Mater.*, 1998, **10**, 1191.
29 T. V. Misuryaev, T. V. Murzina, O. A. Aktsipetrov, N. E. Sherstyuk, V. B. Cajipe and X. Bourdon, *Solid State Commun.*, 2000, **115**, 605.
30 J. H. Liao, G. Marking, K. Hsu, Y. Matsushita, M. Ewbank, R. Borwick, P. Cunningham, M. Rosker and M. Kanatzidis, *J. Am. Chem. Soc.*, 2003, **125**, 9484.
31 J. W. Lekse, M. A. Moreau, K. L. McNerny, J. Yeon, P. S. Halasyamani and J. A. Aitken, *Inorg. Chem.*, 2009, **48**, 7516.
32 L. Geng, W. D. Cheng, C. S. Lin, W. L. Zhang, H. Zhang and Z. Z. He, *Inorg. Chem.*, 2011, **50**, 5679.
33 D. Mei, W. Yin, K. Feng, Z. Lin, L. Bai, J. Yao and Y. Wu, *Inorg. Chem.*, 2011, **51**, 1035.
34 H. Lin, L. J. Zhou and L. Chen, *Chem. Mater.*, 2012, **24**, 3406.
35 D. Mei, W. Yin, K. Feng, Z. Lin, L. Bai, J. Yao and Y. Wu, *Inorg. Chem.*, 2012, **51**, 1035.
36 W. Yin, K. Feng, R. He, D. Mei, Z. Lin, J. Yao and Y. Wu, *Dalton Trans.*, 2012, **41**, 5653.
37 J. I. Jang, S. Park, C. M. Harrison, D. J. Clark, C. D. Morris, I. Chung and M. G. Kanatzidis, *Opt. Lett.*, 2013, **38**, 1316.
38 S. M. Kuo, Y. M. Chang, I. Chung, J. I. Jang, B. H. Her, S. H. Yang, J. B. Ketterson, M. G. Kanatzidis and K. F. Hsu, *Chem. Mater.*, 2013, **25**, 2427.
39 J. A. Brant, D. J. Clark, Y. S. Kim, J. I. Jang, J.-H. Zhang and J. A. Aitken, *Chem. Mater.*, 2014, **26**, 3045.
40 X. Li, C. Li, P. Gong, Z. Lin, J. Yao and Y. Wu, *J. Mater. Chem. C*, 2015, **3**, 10998.
41 B.-W. Liu, H.-Y. Zeng, M.-J. Zhang, Y.-H. Fan, G.-C. Guo, J.-S. Huang and Z.-C. Dong, *Inorg. Chem.*, 2015, **54**, 976.
42 B.-W. Liu, H.-Y. Zeng, X.-M. Jiang, G.-E. Wang, S.-F. Li, L. Xu and G.-C. Guo, *Chem. Sci.*, 2016, **7**, 6273.
43 K. Wu, Z. Yang and S. Pan, *Angew. Chem., Int. Ed.*, 2016, **55**, 6713.
44 K. Wu, Z. Yang and S. Pan, *Chem. Commun.*, 2017, **53**, 3010.
45 S. Das, C. Ghosh, S. Gangopadhyay, Y. M. Andreev and V. V. Badikov, *Jpn. J. Appl. Phys.*, 2006, **45**, 5795.
46 O. M. Yurchenko, I. D. Olekseyuk and O. V. Parasyuk, *J. Cryst. Growth*, 2005, **275**, e1983.
47 V. Petrov, V. Badikov, G. Shevyrdyaeva, V. Panyutin and V. Chizhikov, *Opt. Mater.*, 2004, **26**, 217.
48 W. Yin, K. Feng, W. Hao, J. Yao and Y. Wu, *Inorg. Chem.*, 2012, **51**, 5839.
49 Y. Kim, I. S. Seo, S. W. Martin and J. Baek, *Chem. Mater.*, 2008, **20**, 6048.
50 R. W. Boyd, *Nonlinear optics*, Academic press, 2003.
51 D. Ristau, *Laser-induced damage in optical materials*, CRC Press, 2014.
52 G.-C. Guo, Y. Yao, K. Wu, L. Wu and J. Huang, *Prog. Chem.*, 2001, **13**, 151.
53 S.-P. Guo, Y. Chi and G.-C. Guo, *Coord. Chem. Rev.*, 2017, **335**, 44.
54 B.-W. Liu, M.-Y. Zhang, X.-M. Jiang, S.-F. Li, H.-Y. Zeng, G.-Q. Wang, Y.-H. Fan, Y.-F. Su, C. Li, G.-C. Guo and J.-S. Huang, *Chem. Mater.*, 2017, **29**, 9200.
55 I. D. Brown, *Struct. Bonding*, 2014, **158**, 11.
56 C. D. Morris, I. Chung, S. Park, C. M. Harrison, D. J. Clark, J. I. Jang and M. G. Kanatzidis, *J. Am. Chem. Soc.*, 2012, **134**, 20733.
57 I. Chung, J.-H. Song, J. I. Jang, A. J. Freeman and M. G. Kanatzidis, *J. Solid State Chem.*, 2012, **195**, 161.
58 A. S. Haynes, F. O. Saouma, C. O. Otieno, D. J. Clark, D. P. Shoemaker, J. I. Jang and M. G. Kanatzidis, *Chem. Mater.*, 2015, **27**, 1837.
59 *Rigaku CrystalClear, 1.3.5*, Rigaku Corp., Tokyo, 2002.
60 G. Sheldrick, *SHELXS-97, program for X-ray crystal structure solution*, University of Göttingen, Germany, 1997.

61 A. Spek, Single-crystal structure validation with the program PLATON, *J. Appl. Crystallogr.*, 2003, **36**, 7–13.
62 S. Kurtz and T. J. Perry, *Appl. Phys.*, 1968, **39**, 3798.
63 M.-J. Zhang, X.-M. Jiang, L.-J. Zhou and G.-C. Guo, *J. Mater. Chem. C*, 2013, **1**, 4754.
64 M. C. Payne, M. P. Teter, D. C. Allan, T. A. Arias and J. D. Joannopoulos, *Rev. Mod. Phys.*, 1992, **64**, 1045.
65 S. J. Clark, M. D. Segall, C. J. Pickard, P. J. Hasnip, M. I. Probert, K. Refson and M. C. Payne, *Z. Kristallogr.*, 2005, **220**, 567.
66 F. P. Bassani and G. P. Parravicini, *Electronic States and Optical Transitions in Solids*, Pergamon Press Ltd., Oxford, 1975, pp. 149–154.
67 M. Gajdoš, K. Hummer, G. Kresse, J. Furthmüller and F. Bechstedt, *Phys. Rev. B*, 2006, **73**, 045112.
68 K. Wu, Z. Yang and S. Pan, *Inorg. Chem.*, 2015, **54**, 10108.
69 D. Mei, W. Yin, Z. Lin, R. He, J. Yao, P. Fu and Y. Wu, *J. Alloys Compd.*, 2011, **509**, 2981.
70 H. Lin, L. Chen, L. J. Zhou and L. M. Wu, *J. Am. Chem. Soc.*, 2013, **135**, 12914.
71 J. Tarascon, G. Hull and J. Waszczak, *Mater. Res. Bull.*, 1985, **20**, 935.
72 J. C. Jumas, E. Philippot and M. Maurin, *J. Solid State Chem.*, 1975, **14**, 152.
73 A. Rothenberger, H. H. Wang, D. Chung and M. G. Kanatzidis, *Inorg. Chem.*, 2010, **49**, 1144.
74 K. M. Ok, *Acc. Chem. Res.*, 2016, **49**, 2774.
75 H. Jo, S.-J. Oh and K. M. Ok, *Dalton Trans.*, 2017, **46**, 15628.
76 S.-F. Li, X.-M. Jiang, B.-W. Liu, D. Yan, C.-S. Lin, H.-Y. Zeng and G.-C. Guo, *Chem. Mater.*, 2017, **29**, 1796.
77 I. Bodnar and N. Orlova, *Phys. Status Solidi A*, 1985, **91**, 50.
78 J. P. Perdew and M. Levy, *Phys. Rev. Lett.*, 1983, **51**, 1884.
79 J. P. Perdew, J. A. Chevary, S. H. Vosko, K. A. Jackson, M. R. Pederson, D. J. Singh and C. Fiolhais, *Phys. Rev. B: Condens. Matter Mater. Phys.*, 1992, **46**, 6671.